Gassing During Tapping of Silicon

KURIAN J. VACHAPARAMBIL [ID],[1] BALRAM PANJWANI,[1]
and JAN ERIK OLSEN [ID][1,2]

1.—SINTEF, Trondheim, Norway. 2.—e-mail: Jan.E.Olsen@sintef.no

During tapping of metal from silicon furnaces, a significant amount of gas is often released through the tap-hole. The gas is combustible, and a flame jet is created which poses a safety threat to operators. Due to the high temperatures involved, thermal NOx is also produced. This is a threat to the environment and the health of the operators. These phenomena, known as gassing, have been studied here by a mathematical model for reactive turbulent flows. The results show that the flame jet can extend several meters out from the tap-hole, and that the strength of the flame jet increases with the amount of gassing. The simulations also show that the NOx production increases with the amount of gas exiting the tap-hole, and that the thermal NOx formation does not substantially impact the length of the gas jet.

INTRODUCTION

Tapping of metal and other products from metallurgical furnaces is the process step in which products are transferred from the furnace to a ladle for further downstream processing. The process step is important for both furnace operation and downstream logistics.[1] Tapping of silicon and ferrosilicon faces an additional challenge compared to other metal furnaces: strong gas jets are emitted through the tap-hole, exposing operators to high risks. The focus of this study is on tapping of silicon and ferrosilicon (hereafter silicon) and gassing from the tap-hole.

Tapping of metallurgical furnaces have been extensively studied and is well presented in the literature.[1] Most of the literature addresses tapping of blast furnaces, but submerged arc furnaces have also been studied. Findings on tapping of silicon furnaces, however, are less frequently reported. Tveit et al.[2] described the most important problems and challenges in the tapping process in silicon production. The possible impact of improper draining of the silicon furnace was described, as well as some root causes of the formation of the tapping gas. Kadhkodabeigi et al.[3] investigated the ability of a new hood system (for Elkem) to extract the combustion products from the tap-hole gas jet. Kadhkodabeigi et al.[4] studied tapping of molten silicon and found that the flow in the tap-hole is highly dependent on the conditions inside the furnace. They found an increase in tapping flow rates with increasing crater pressure in a submerged-arc furnace. Tangstad et al.[5] presented a conceptual model on Si/FeSi tapping, in addition to discussing findings from excavations and how furnace conditions could influence tapping of furnaces and drainage from the back electrodes. CFD modeling applied by Olsen et al.[6] to study flow of gas and metal through the tap-hole found that burden permeability affects gassing (the flow rate) and the magnitude of crater pressure.

Most of the existing studies in the literature deal with the drainage of the furnace and predictions of metal and gas rates out of the tap-hole, while the reactive nature of tap-hole gas jets is seldom investigated. To address this lack of knowledge, we apply CFD to primarily study how the gas emitted from the tap-hole reacts with the atmosphere outside the furnace to create a hazardous gas jet. In this study, the focus is on the reactive single-phase flow of the gas emitted from the tap-hole.

SILICON PROCESS

Silicon is produced in submerged arc furnaces by adding quartz (SiO_2), and carbon-rich materials, like coke, coal, charcoal, and wood chips (C), from the top of the furnace. The raw materials react according to the overall reaction

$$SiO_2 + (1+y)\ C\ =\ y\ Si\ +\ (1-y)\ SiO \\ +\ (1+y)\ CO$$
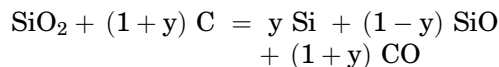
where y is the silicon yield.[7] The energy needed to drive the reaction is supplied via three electrodes submerged in the burden of raw materials and reaction products. The overall reaction consists of multiple step reactions (some of which are endothermic and others exothermic) that complicate the furnace operation, and influences the yield, as the reactions in the furnace are influenced by temperature (see Ref. 7). A silicon furnace with its main features and operating principles is illustrated in Fig. 1. It should be noted that many furnaces operate with a rotating furnace shell with tapping performed continuously or in batches.

The flow of metal and gases in the furnace is driven by gravity and gas pressure. This flow of gases and liquid metal is resisted by the particle bed, and by zones of low permeability (see discussion in Ref. 6). A crater is formed underneath the electrodes, where electric arcs spark between the electrode tip and the metal pool at the bottom of the furnace. Highly viscous melted silica (SiO_2) drains downwards at the outside of the crater, forming a sticky crater wall together with the particles in the burden. The permeability of the crater wall is lower than the permeability of the main bulk of the burden. A condensate layer, which is sticky and has a low permeability, is formed higher up in the furnace where SiO gas is cooled. This condensate layer tends to make the overall permeability of the burden lower than the burden of submerged arc furnaces for other alloys and metals.

Due to the high temperature within the reaction zone of the furnace and the added flow resistance from the low permeability, there is a heightened pressure of gases in the crater/cavity region when compared to the surroundings.[3,6] This gives an extra force to drive the metal and gas out of the furnace. While the metal normally only drains through the tap-hole, gas will escape through both the top of the furnace and the tap-hole. The area of the furnace top is much greater than the tap-hole opening, and thus most gas leaves through the top. The tap-hole opening area is roughly only 0.01% of the top area. Since the burden is relatively dense, there is some resistance to the flow upwards through the top, forcing gases through the tap-hole. Compared to furnaces for other alloys and metals, more gas exits the tap-hole in silicon furnaces. This causes a safety issue since the gas is combustible (see Ref. 3).

If we assume a reasonable yield of 0.9 in the overall reaction, stoichiometry dictates that, for a production of 100 tonnes/day of Si (which is typical of a 40-MW furnace), 226 tonnes/day, or 2.6 kg/s, of gas is produced with a mass fraction of 0.075 of SiO.[7] If 2% of the gas leaves through the tap-hole, the gas rate through the tap-hole is 0.05 kg/s. It must be noted that the numbers used above are averaged values, which in normal operations vary quite significantly. The molten metal has been measured to leave the tap-hole with temperatures in the order of 2000 K, so it is reasonable to assume the same temperature for the gas.

The tap-hole gasses, consisting of CO and SiO, react with ambient air consisting of N_2 and O_2 (in addition to small amounts of argon) to produce CO_2 and SiO_2, based on the following reactions[8]:
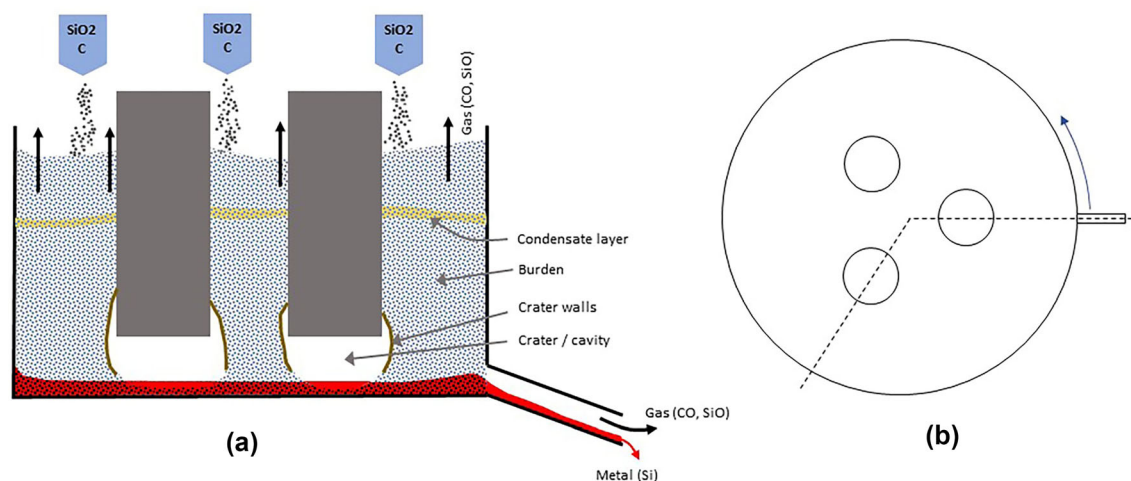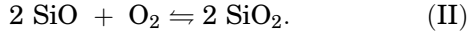
$$2\ CO\ +\ O_2\ \leftrightharpoons\ 2\ CO_2, \qquad (I)$$

Fig. 1. Vertical (a) and horizontal (b) cross-sections of a simplified typical silicon furnace. The vertical cross-section is given by the dashed line in the horizontal cross-section.

$$2\ SiO\ +\ O_2 \rightleftharpoons 2\ SiO_2. \qquad (II)$$

These reactions are exothermic and create a flame of high temperature at the tap-hole, which results in the formation of nitrous oxides (NOx), commonly referred to as thermal NOx, which adversely impact human health and the environment.[8,9] The thermal NOx, which predominately consist of NO, is generated by two reactions described by the Zeldovich mechanism (see Ref. [9]):

$$O\ +\ N_2 \rightleftharpoons NO\ +\ N, \qquad (III)$$

$$N\ +\ O_2 \rightleftharpoons NO\ +\ O. \qquad (IV)$$
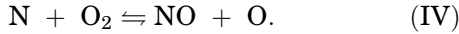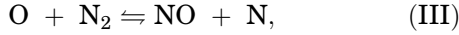
In a simplified form, the thermal NOx formation can be described by a global NO formation reaction, which combines the two reactions of the Zeldovich mechanism:

$$N_2 +\ O_2 \rightleftharpoons 2\ NO. \qquad (V)$$
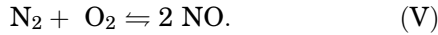
MATHEMATICAL MODEL

The combustion of the tap-hole gas jet has been modeled using rhoReactingBuoyantFoam (a turbulent reacting flow solver available in OpenFOAM 8[10]), which solves conservation equations of mass, momentum, and energy and transport equations for the relevant chemical species:

$$
\begin{aligned}
&\frac{\partial \rho}{\partial t} + \nabla \cdot (\rho \vec{U}) = 0 \\
&\frac{\partial}{\partial t}\left(\rho \vec{U}\right) + \nabla \cdot \left(\rho \vec{U}\vec{U}\right) = -\nabla p_{\text{rgh}} - \vec{g} \cdot \vec{x}\nabla \rho + \nabla \cdot \tau \\
&\frac{\partial}{\partial t}(\rho Y_i) + \nabla \cdot \left(\rho \vec{U}Y_i\right) + \nabla \cdot \vec{J}_i = \dot{w}_i \\
&\frac{\partial}{\partial t}(\rho h_s) + \nabla \cdot \left(\rho \vec{U}h_s\right) + \frac{\partial}{\partial t}(\rho K) + \nabla \cdot \left(\rho \vec{U}K\right) \\
&\quad - \frac{\partial p}{\partial t} + \nabla \cdot \vec{J}_s = \dot{Q}_r + \dot{Q}_{\text{rad}}
\end{aligned}
$$

$$(1.1)$$

where ρ is the mixture density, $\vec{U}$ is the velocity, p is the pressure, and $p_{\text{rgh}} = p - \rho\vec{g} \cdot \vec{x}$, τ is the viscous stress tensor, $\vec{g}$ is gravity, Y_i is the mass fraction of species (i), h_s is the sensible enthalpy, and K is the specific kinetic energy. In Eq. 1.1, $\vec{J}_i$ is the diffusion flux calculated based on Fick's 1st law, with species diffusivity approximated based on momentum diffusivity, and $\vec{J}_s$ is the heat flux vector calculated based on conductive heat transfer and neglecting the effect of species diffusion, see Ref. [11]. In Eq. 1.1, $\dot{w}_i$ corresponds to the generation or consumption of species (i) due to chemical reactions, $\dot{Q}_r$ is the heat generated or consumed due to chemical reactions, and $\dot{Q}_{\text{rad}}$ is a source term in the energy equation related to the radiation. Further details of the

governing equations used by the reacting flow solvers in OpenFOAM are described in Ref. [11]. The equation of state used to describe the dependence between density, temperature, and pressure is based on a perfect gas model.[10] The transport properties, like the dynamic viscosity and thermal conductivity of each species, have been calculated using the Sutherland viscosity model and the modified Eucken correlation, respectively.[9,12] The thermodynamic properties of the species are calculated based on the NASA 7-coefficient polynomials, which are defined for two temperature ranges[13] (see supplementary Table S1 in the online supplementary material).

The turbulence in the gas jets has been modeled using a k–ω SST model which involves solving for turbulent kinetic energy (k) and turbulent specific dissipation rate (ω) (see Ref. [14] for more details). As the flow is highly turbulent, the interaction between turbulence and chemical kinetics is treated using the Eddy Dissipation Concept (EDC) proposed by Ref. [15]. The EDC model, which assumes that chemical reactions occur within the 'fine structures' or the smallest scales of turbulence, includes finite-rate chemistry to estimate $\dot{w}_i$ (see Ref. [15–17]). The kinetics of the reactions are estimated based on the Arrhenius equation, $k_f = AT^{\beta}\exp(-T_a/T)$, where A is pre-exponent factor, T_a is the activation temperature, and β is the temperature exponent.[17] The reaction kinetics data of CO and SiO combustion used in this work are tabulated in Table I. It should be noted that OpenFOAM computes the backward reaction rate constant of a given reaction at run-time, based on the computed forward and equilibrium reaction rate constants, which means that the user needs to provide the pre-exponent factor, activation temperature, and temperature exponent just for the forward reaction (as shown in Table I).

The thermal NOx formation can be described by the Zeldovich mechanism,[9] as briefly described in the previous section, which consists of two reactions involving N_2, O_2, N, and O. To simulate the formation of thermal NOx involves solving for the transport equations of the O and N radicals, as well as the N_2 and O_2 molecules, in addition to using a detailed reaction scheme, discussed in, Ref. [8] which complicates the model and increases the

Table I. The forward reaction kinetics parameters for SiO and CO combustion reactions in m^3, kmol, and K

	A	β	T_a
2 CO + O_2 $\rightleftharpoons$ 2 CO_2 (I)	2.24e12	0.0	2403.51022
2 SiO + O_2 $\rightleftharpoons$ 2 SiO_2 (II)	1.00e12	0.0	0.12077941

The tabulated data is obtained after conversion to compatible units from Ref. [8].

computational overhead. A pragmatic approach to model NO formation is to use the global reaction $N_2 + O_2 \rightleftharpoons 2\,NO$ or (reaction V). Since the kinetics of this global reaction is not available in the literature, to the best knowledge of the authors, the reaction rate of this reaction is assumed to be bound between the upper and lower reaction rates of the two reactions in the Zeldovich mechanism, as tabulated in Table II.

The radiative heat transfer is considered using Finite Volume Discrete Ordinate Method (fvDOM) radiation model which solves radiative transfer equations (RTE) to obtain radiation intensity as a function of location and direction vectors.[18] The fvDOM model also accounts for absorption of radiation by gases based on species-specific temperature-dependent polynomials, which are used to describe the mean absorption coefficient (see Ref. 19) of CO_2, SiO_2, SiO, O_2, and N_2;, further information is included in the supplementary Table S3. The source/sink term in the conservation of energy related to the effect of radiation, $\dot{Q}_{rad}$, is calculated based on the divergence of the radiative flux as described in Ref. 20.

The governing equations are solved for the pseudo-steady solution and discretization schemes used are based on,[10,21] and summarized in the supplementary Tables S4–S6. The convergence criteria used in the simulation are set based on universal absolute tolerance of $1e-6$ (but a non-zero relative tolerance of 0.1 is used for velocity, sensible enthalpy, and the turbulence terms like k and ω)[22] with an under-relaxation factor for equations set to 0.9 (see Ref. 23). The convergence of the solution is assumed when the values of the molar flow rate of CO and SiO through the tap-hole agree reasonably with the molar outflow of CO_2 and SiO_2 through the outlets over a range of iterations (a deviation below 5% is accepted).

MODELING STUDY

The nature of the gas jet emanating from the tap-hole has been studied by the model presented above. The computational domain includes the tap-hole and a box representing the zone outside the furnace. This is illustrated in the left part of Fig. 2. Gas is injected through the tap-hole with an inlet velocity as the boundary conditions, where flow rate, temperature, and composition of the gas is specified (the red region in Fig. 2). The furnace wall is a no-slip wall with a zero gradient temperature condition (the gray surfaces in Fig. 2). A small zone (0.03 × 0.2 m^2) at the furnace wall underneath the tap-hole is given an elevated temperature to represent the radiation from the metal being poured out of the tap-hole (the green rectangle in Fig. 2). At the outlet (top and end of domain—identified as yellow surfaces in Fig. 2), a zero-gradient condition is applied for the outflow and, in case of any inflow, a fixed value is specified. For the sides and bottom (the surroundings—identified as white/transparent surfaces in Fig. 2), an inlet (with specified mass flow rate, temperature, and standard air composition of species) is applied, since that enhances convergence and allows for the study of wind effects. Note that a series of inlet rates for the surrounding air was tested and a sufficiently low value was chosen which does not affect the flow field of the emanating gas jet. The different tap-hole mass flow rate and gas composition values used in the parametric study discussed in this work are summarized in Table III along with a summary of the boundary conditions used. It should be stated that the combustion of the tap-hole occurs in an air (or oxidizer)-rich environment, as the mass flow rate of air (= 3 kg/s) is much larger than the mass flow rate of the tap-hole gases, which is substantially low (between 0.05 kg/s and 0.1 kg/s). The turbulent characteristics of the inflow through the tap-hole is given by turbulent intensity for turbulent kinetic energy (k) which is set to be equal to 8%, and the mixing length (length scale for turbulent momentum transfer) for ω is set equal to a value much smaller than the tap-hole diameter (arbitrarily chosen to be 0.735 mm).

Mesh convergence was investigated by comparing the results from three meshes with nearly 0.65 million, 1.1 million, and 4.72 million cells, respectively, for the case with a gas flow rate of 0.1 kg/s and SiO mass fraction of 0.05. All three grids were made of hexahedral cells. To verify mesh convergence, the isotherm of 1500 K (which is averaged over the last 10,000 iterations) was used for comparison of the results from the simulations using the three grids as seen in Fig. 3. Since there is good agreement between the isosurfaces between the two finest grids, the second finest grid (with nearly 1.1 million cells) was used in the simulations discussed in this study.

RESULTS

With the case setup defined in III, a series of simulations were performed for different inlet flow rates and inlet mass fractions of SiO/CO. Each inlet mass flow rate represents a different inlet velocity, which results in spatially different velocity fields after the tap-hole, as seen in the contour plots in

Table II. The forward reaction kinetics parameters for global NO formation reactions in m^3, kmol, and K

	A	β	T_a
$O + N_2 \rightleftharpoons NO + N$ (III)	1.8e11	0.0	38370
$N + O_2 \rightleftharpoons NO + O$ (IV)	1.8e7	1.0	4680

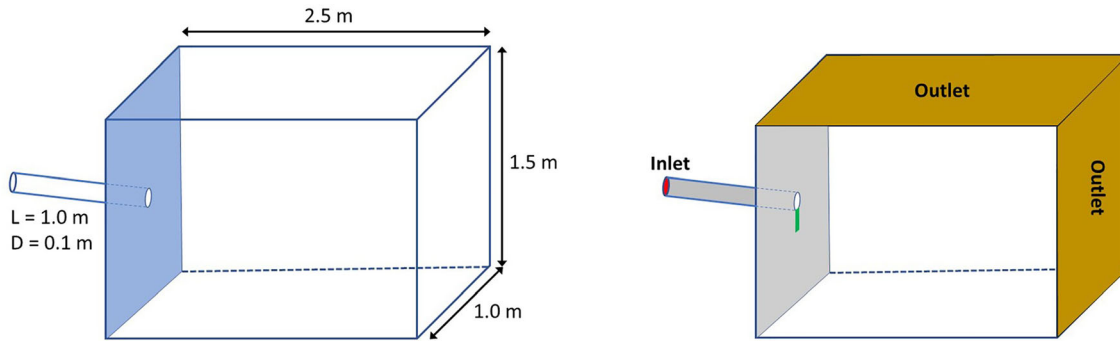The tabulated data is obtained after conversion to compatible units from Ref. 9

Fig. 2. Geometry of domain with dimensions (left) and boundary conditions (right). Boundary conditions are velocity inlet (red), pressure outlet (brown), walls (gray), wall section with elevated temperature (green), and surrounding flow (white/transparent) (Color figure online).

Table III. Case definition (boundary conditions)

|	
Inlet	Mass flow rate: 0.05, 0.075, 0.1 kg/s Mass fraction of SiO: 0.05, 0.1, 0.15 Mass fraction of CO: 0.95, 0.9, 0.85 Mass fraction of remaining species: 0.0 Turbulent intensity of 8% with a mixing length of 0.735 m Temperature: 2000 K with gray-diffuse condition for radiation intensity
Wall sections with elevated temperature	Zero gradient for all species and p_{rgh} Wall functions conditions and no-slip for velocity Temperature: 2000 K with grey-diffuse condition for radiation intensity
Walls	Zero gradient for all species, temperature and p_{rgh} The gray-diffuse condition is used for radiation intensity Wall functions conditions and no-slip for velocity
Pressure outlet	Zero gradient for outflow (and fixed value for any inflow used is specified for each parameter within brackets): Ar (0.01), N_2 (0.76), O_2 (0.23), remaining species (0.0) and velocity (zero normal and tangential inflow velocity) The gray-diffuse condition for radiation intensity Constant total pressure of 101325 Pa for p_{rgh}
Surrounding flow	Mass flow rate: 1 kg/s Mass fraction of Ar, N_2, O_2: 0.01, 0.23, 0.76 Mass fraction remaining species: 0.0 Turbulent intensity of 8% with a mixing length of 0.735 m Temperature: 310 K with gray-diffuse condition for radiation intensity
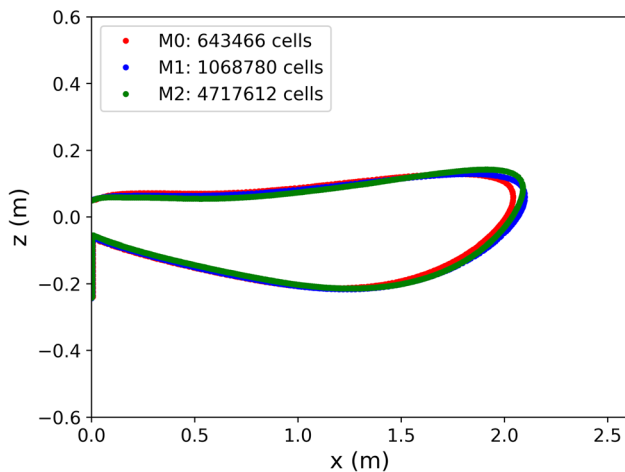
Fig. 3. Mesh convergence shown based on 1500 K isosurface of temperature.

Fig. 4. The maximum velocity reaches up to 87 m/s for the case with the highest mass flow rate. Such high velocities of the tap-hole gas jets are not unrealistic when compared against operator observations and earlier studies.[2,3] The flow decelerates shortly after its release out of the tap-hole, where it is allowed to expand. The expansion of the gas-jet results in reducing its momentum, and eventually the influence of buoyancy of the gases (caused by the reduction in density due to high temperatures) becomes dominant. This results in the upwards bend of combusting jets after a distance from the tap-hole: the higher the inlet velocity of the tap-hole gases, the further away the bending of the jet occurs from the tap-hole.

Due to the exothermic nature of the CO and SiO combustion reaction mechanisms, the temperature increases in the region outside the tap-hole, as seen in Fig. 5. The temperature is seen to rise to 2700 K
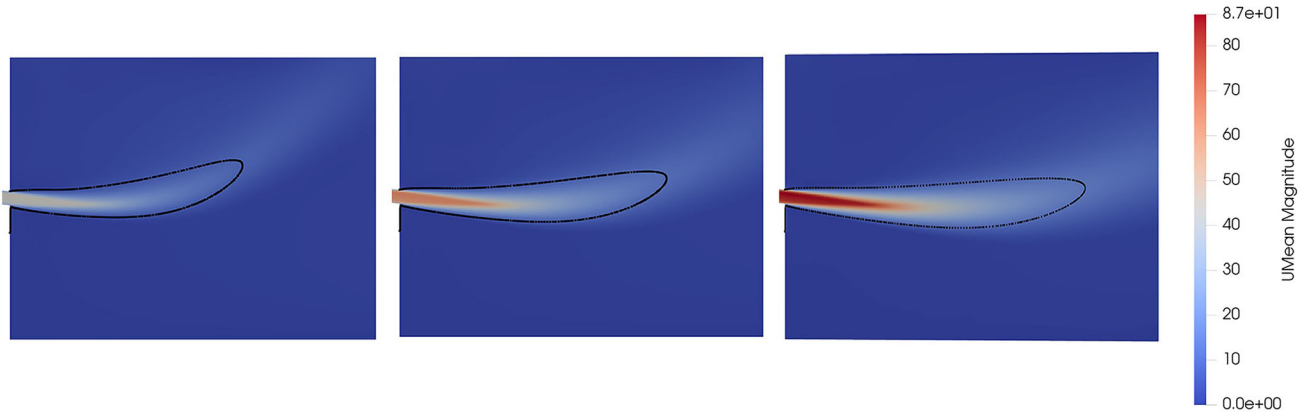
Fig. 4. Contours of velocity magnitude (in m/s) with 1500 K isosurface for gas rates of 0.05 kg/s (left), 0.075 kg/s (middle) and 0.100 kg/s (right) and inlet SiO mass fraction of 0.05. The black line is the 1500 K isotherm (Color figure online).
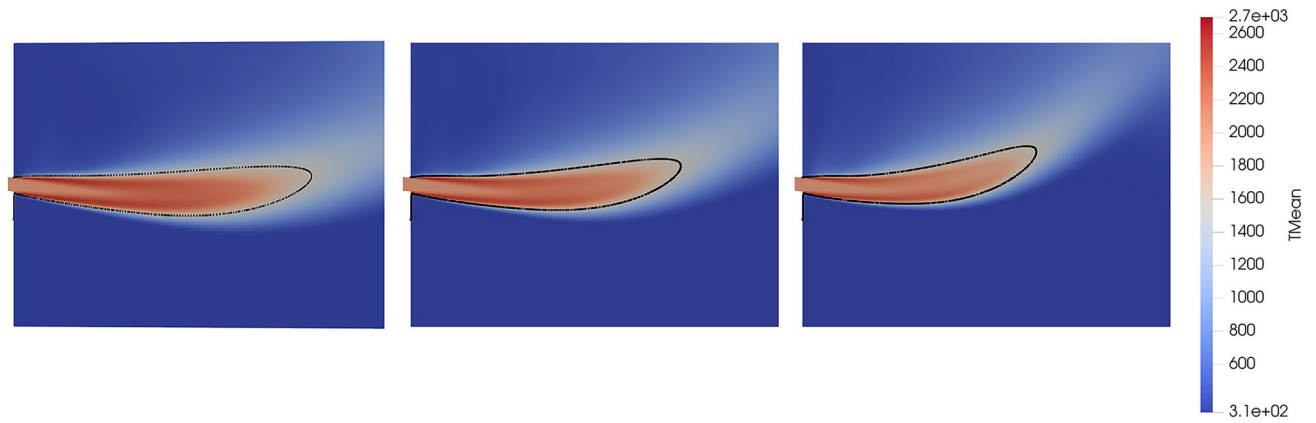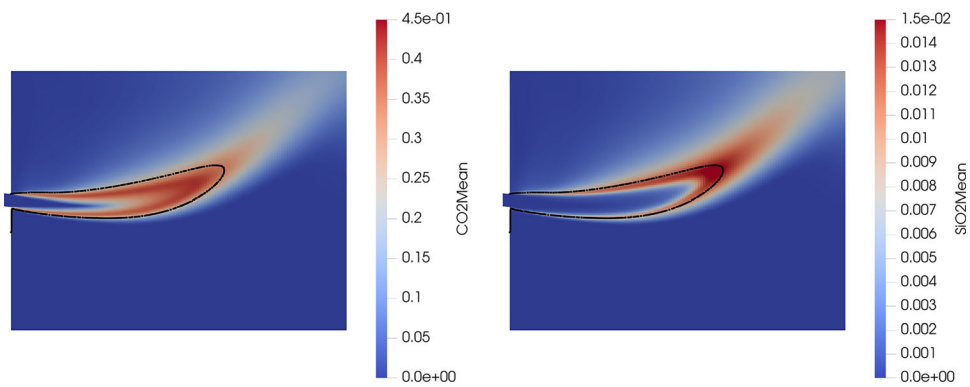

Fig. 5. Temperature contours (in K) with 1500 K isosurface for gas rates of 0.100 kg/s (left), 0.075 kg/s (middle) and 0.050 kg/s (right) and inlet SiO mass fraction of 0.05. The black line is the 1500 K isotherm (Color figure online).

Fig. 6. Contours CO_2 and SiO_2 mass fractions for inlet flow rate of 0.05 kg/s and inlet mass fraction of SiO of 0.05. The black line is the 1500 K isotherm (Color figure online).
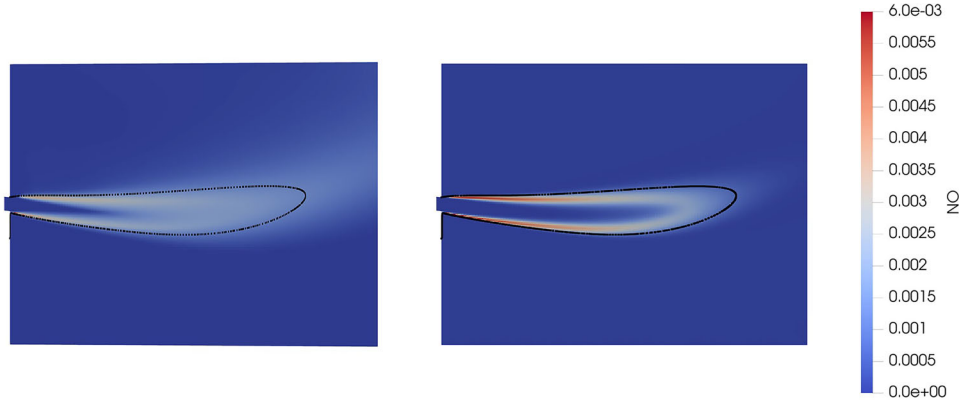
Fig. 7. Contours of NO mass fraction inlet flow rate of 0.1 kg/s and inlet mass fraction of SiO of 0.05 with assumption of kinetics from O + N$_2$ NO + N or reaction III (left) and N + O$_2$ NO + O or reaction IV (right). The black line in the figures is the 1500 K isotherm (Color figure online).

from 2000 K at the inlet. Higher gas rates produce larger flames and subsequently larger regions with high temperatures.

Contour plots of CO$_2$ and SiO$_2$ mass fractions are shown in Fig. 6. An interesting result from the simulation is the two rather distinct regions, at which CO and SiO combustion seems to occur in the gas jet flame. This could be attributed to the faster reaction rate of SiO combustion when compared to CO combustion, due to the higher activation temperature of the latter reaction (see Table I).

Contour plots of NO mass fractions for the two different assumptions on reaction kinetics (tabulated in Table II) are shown in Fig. 7. The figure qualitatively shows that lower amounts of NO are transported from the flame towards the outlets when the global reaction mechanism used the kinetics of N + O$_2$ ⇌ NO + O (or reaction IV) in comparison to when the kinetics of O + N$_2$ ⇌ NO + N (or reaction III) was used. This is somewhat contradictory to the kinetic coefficients of these reactions tabulated in Table II, and can be attributed to the fast reverse reaction rate of reaction IV when compared to reaction III. At equilibrium, when the forward and reverse reaction rates are equal, the reverse reaction rate constant (k_r) can be estimated using the equilibrium constant (k_c) and forward reaction rate constant (k_f) for the global NO reaction:

$$k_f[N_2][O_2] = k_r[NO]^2 \Rightarrow \frac{k_f}{k_r} = \frac{[NO]^2}{[N_2][O_2]} = k_c \Rightarrow k_r = \frac{k_f}{k_c}.$$
(1.2)

Since the equilibrium constant is dependent only on the reactants and products, and is independent of the reaction kinetics, the equilibrium constant of the global NO reaction is the same using kinetics of both reaction III and reaction IV. Thus, the ratio of the reverse and forward reaction kinetics of reaction III and reaction IV can be estimated as:

$$\frac{k_r|_{\text{governed by reaction III}}}{k_r|_{\text{governed by reaction IV}}} = \frac{\dfrac{k_f|_{\text{governed by reaction III}}}{k_c}}{\dfrac{k_c}{k_f|_{\text{governed by reaction IV}}}}$$

$$= \frac{k_f|_{\text{governed by reaction III}}}{k_f|_{\text{governed by reaction IV}}}$$

$$= \frac{10^4}{T} e^{-33690/T}.$$
(1.3)

This ratio of the reverse and forward kinetics of reaction III and reaction IV is much smaller than 1, which means that, with the kinetics of reaction IV, NO is formed quickly, and subsequently the reversible reaction splits the NO to form N$_2$ and O$_2$ (when compared to reaction III). So, the NO formation is governed predominantly by the kinetics of reaction III or O + N$_2$ ⇌ NO + N, due to its slower kinetics (see discussion in Ref. 9).

Another parameter of interest in tap-hole gas jets is the length of these jets as it directly affects the personal working near the tap-hole. In this study, we define the length of the gas jet as the extension of the 1500 K isosurface into the domain. The choice of 1500 K to investigate the tap-hole flame length represents a critically high temperature which can cause damage. It should be noted that this length is not an indication of a 'safe' distance from the tap-hole, but a parameter to compare the length scale of the different scenarios considered in this work. The length of the tap-hole gas jets is observed to increase with larger tap-hole exit mass flow rate and higher amounts of CO (or lower amounts of SiO) (see Fig. 8). The NOx kinetics have been observed to not substantially impact the length of the gas jets in these simulations.
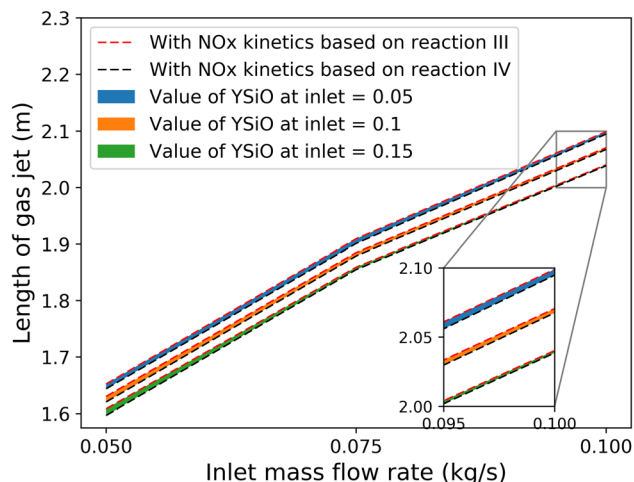
Fig. 8. Length of gas jet defined by the 1500 K isotherm as a function of gas tap-hole exit rates for various gas compositions as well as NO kinetics based on reaction III $(O + N_2 \rightleftharpoons NO + N)$ and reaction IV $(N + O_2 \rightleftharpoons NO + O)$.
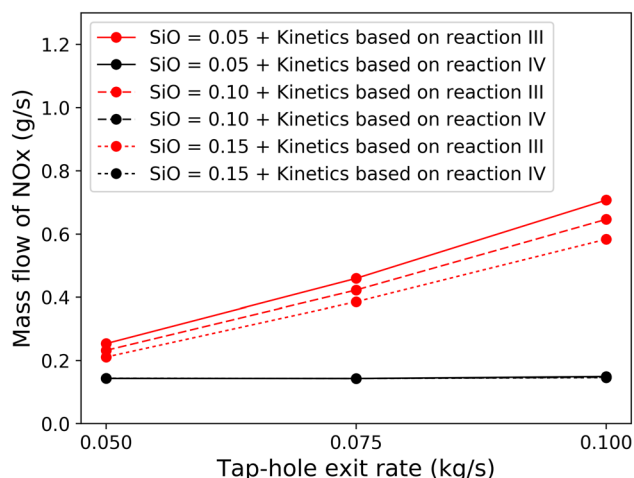

Fig. 9. NOx or NO obtained at outlet as a function of tap-hole exit rate and gas composition (based on mass fraction of SiO) as well as NO kinetics: reaction III $(O + N_2 \rightleftharpoons NO + N)$ and reaction IV $(N + O_2 \rightleftharpoons NO + O)$

A similar plot has been made for the mass flow of NOx as a function of tap-hole exit rate of gas, as shown in Fig. 9. This is in principle the NOx production. The results are somewhat inconclusive since the exact kinetics have not been applied. The results indicate a range between which we expect to find the production of NOx.

CONCLUSION

The reactive flow of the tap-hole gas jet from silicon furnaces has been simulated using rhoReactingBuoyantFoam solver in OpenFOAM. The simulations included three global reactions which governs the combustion of CO and SiO as well as generation of thermal NOx, i.e., NO. Since kinetics of the global reaction for NOx is not available in literature, the kinetics data available for the Zeldovich mechanism were used to simulate the upper and lower limits of the NOx formation. The simulations of tap-hole gassing were performed for a range of tap-hole exit gas flow rates and compositions. The main conclusions from the studies performed are

- Longer tap-hole gas jets are observed for larger values of tap-hole exit flow rates and higher amounts of CO (or lower values of SiO). The influence of NOx kinetics on the tap-hole gas jet length is not substantial.
- When buoyancy effect become dominant compared to inertial effects, an upwards bend of the flame is observed after some distance from the tap-hole. This upwards bend of the flame is closer to the tap-hole for lower tap-hole exit rate of the gases.
- CO and SiO combustion have been observed to occur on two distinct regions of the flame due to the faster kinetics of the latter reaction.
- NOx generation is dominated by slower $O + N_2 \rightleftharpoons NO + N$ when compared to the faster $N + O_2 \rightleftharpoons NO + O$. Since $N + O_2 \rightleftharpoons NO + O$ has a very high forward and reverse reaction rate, when its kinetics was used in the global NOx mechanism, it generated less NOx than the slower mechanism kinetics. More NOx is generated with larger tap-hole exit mass flow rates and higher amounts of CO. Using the global NOx reaction with the two-reaction kinetics to obtain the upper and lower bounds of the NOx generated provided an overall trend of NOx formation during gassing of silicon. For accurate determination of the NOx produced in these phenomena, treatment for the N and O radicals either using a detailed reaction mechanism (discussed in Ref. 8) or using assumptions (like equilibrium of the oxygen dissociation–recombination step) to obtain the distribution of these radicals (see Ref. 9 for more details) is required.
- Obviously, it can be stated that the gassing hazards will reduce if less gas is allowed to exit through the tap-hole.

As we have investigated the influence of a range of tap-hole gas composition and flow rate for a generic tap-hole geometry using a single-phase reactive flow approach, there are some topics which should be further investigated to develop a comprehensive understanding of these reactive gas jets:

- The influence of the various tap-hole geometries on the shape and size of these gas jet
- Impact of the turbulence conditions (at the entrance of the tap-hole) on the nature of the tap-hole gas jets

Finally, the modeling used in the current work does not consider the impact of microsilica particles formed during the phenomena.

CONFLICT OF INTEREST

The authors confirm that there exists no conflict of interest with respect to this publication.

SUPPLEMENTARY INFORMATION

The online version contains supplementary material available at https://doi.org/10.1007/s11837-022-05390-1.

REFERENCES

1. L. Nelson and R. Hundermark, *J. S. Afr. Inst. Min. Metall.* https://doi.org/10.17159/2411-9717/2016/v116n5a12 (2014).
2. H. Tveit, T. Halland, K.I. Landrø, S.T. Johansen, and B. Ravary, The tapping process in silicon production. In: *Proceedings of Silicon for the Chemical Industry VI*, Loen, 2002.
3. M. Kadkhodabeigi, H. Tveit, and K. Berget, Silicon process-new hood design for tapping gas collection. In: *Twelfth International Ferroalloys Congress*, Helsinki, 2010.
4. M. Kadkhodabeigi, H. Tveit, and S.T. Johansen, *ISIJ Int.* https://doi.org/10.2355/isijinternational.51.193 (2011).
5. M. Tangstad, E. Ringdalen, J.E. Olsen, K.E. Einarsrud, E. Myrhaug, and Q.G. Reynolds, Conceptual model of tapping mechanisms in FeSi/Si furnaces. In: *16th International Ferro-Alloys Congress (INFACON XVI) 2021, Trondheim/virtual*, 2021.
6. J.E. Olsen, M. Ksiazek, and M. Tangstad, *Furnace tapping 2022* (Springer, New York, 2022).
7. A. Schei, H. Tveit, and J.K. Tuset, *Production of High Silicon Alloys* (Tapir, 1997).
8. B. Panjwani and J. Olsen, Combustion and mechanisms for NOx formation in ferrosilicon electric arc furnaces. In: *European combustion meeting (ECM 2013)*, Lund, 2013.
9. ANSYS, *ANSYS Fluent Theory Guide* (ANSYS Inc., Canonsburg, 2013).
10. C. Greenshields, "OpenFOAM v8 User Guide" (CFD Direct, 2016). https://cfd.direct/openfoam/user-guide-v8/. Accessed from 08 Apr 2022.
11. T. Li, J. Pan, F. Kong, B. Xu, and X. Wang, *Comput. Fluids* 213, 104718 https://doi.org/10.1016/j.compfluid.2020.104718 (2020).
12. B.E. Poling, J.M. Prausnitz, and J.P. O'Connell, *The Properties of Gases and Liquids* (McGraw Hill Professional, New York, 2000).
13. B. McBride, S. Gordon, and M. A. Reno, *Coefficients for Calculating Thermodynamic and Transport Properties of Individual Species* (NASA, 1993).
14. F. Menter, M. Kuntz and R.B. Langtry, Ten years of industrial experience with the SST turbulence model. In: *Fourth International Symposium on Turbulence, Heat and Mass Transfer*, Antalya, 2003.
15. B.F. Magnussen, The eddy dissipation concept a bridge between science and technology. In: *ECCOMAS Thematic Conference on Computational Combustion*, Lisbon, 2005.
16. Z. Li, M. Lewandowski, F. Contino, and A. Parente, *Energy Fuels* 32, 10121 https://doi.org/10.1021/acs.energyfuels.8b01001 (2018).
17. A.H. Kadar, "Modelling Turbulent Non-Premixed Combustion in Industrial Furnaces," (Master thesis at TU Delft, 2015).
18. OpenFOAM, "fvDOM Class Reference", https://www.openfoam.com/documentation/guides/latest/api/classFoam_1_1radiation_1_1fvDOM.html#details. Accessed from 08 Apr 2022.
19. TNF Workshop, "Radiation Models",. https://tnfworkshop.org/radiation/. Accessed from 08 Apr 2022.
20. S.C. Mishra and H.K. Roy, *J. Comput. Phys.* 223, 89 https://doi.org/10.1016/j.jcp.2006.08.021 (2007).
21. G. Maragkos, S. Verma, A. Trouvé, and B. Merci, *Comput. Fluids* 232, 105208 https://doi.org/10.1016/j.compfluid.2021.105208 (2022).
22. D. Christ, Simulating the combustion of gaseous fuels. In: *Presented at 6th OpenFOAM Workshop, Penn State University*, 2011.
23. K. Vachaparambil and K. Einarsrud, *Processes* 7, 542. https://doi.org/10.3390/pr7080542 (2019).